# SUPPORTING INFORMATION

## Nanoarchitectured 2D-2D Heterointerface of Pt@$Ti_3C_2T_x$-rGOAerogels *via* In-Situ γ-Radiolysis Induced Self-Assembly: Interplay between Strain and Ligand Effects in Electrocatalytic Interfaces

Linsha Vazhayal[1‡], Sharon Benny Alex[1‡], Santosh K. Haram[1]*

[1]*Department of Chemistry, Savitribai Phule Pune University, Ganeshkhind, Pune, 411007, India.*

*Corresponding Authors, Email: santosh.haram@unipune.ac.in (Santosh K. Haram)

‡L.V. and S.B.A. contributed equally to this work.

## Table of Content

## I. DETAILS OF EXPERIMENTS AND CALCULATIONS

### S1. Preparation of Graphene Oxide (GO)

GO was prepared according to the modified Hummers' method [1]. In brief, 1 g of graphite powder and 0.5 g of $NaNO_3$ were added into 23.3 mL of concentrated $H_2SO_4$ successively under stirring in an ice bath. Then, 3 g of $KMnO_4$ was slowly added into the above mixture; during which the temperature of the reaction system was kept below 10 °C, and continuously stirred for 1h. The oxidation reaction was allowed to proceed at room temperature for 40 min under stirring. Subsequently, 50 mL of deionized water was slowly added, and the mixture was stirred for another 15 min at 95 °C in an oil bath. Additional 167 mL of water was added, followed by dropwise addition of 5 mL of 30% $H_2O_2$ and the mixture turned from dark brown to bright yellow. The mixture was filtered and washed with aqueous HCl solution (100 mL) three times to remove metal ions. Then, 100 mL of water was used to wash the solid to remove the residual acid. The obtained solid was redispersed in deionized water under stirring and purified by dialysis for 2 weeks. The resultant GO dispersion was then exfoliated by sonication for 30 min and centrifuged for 45 min at 4000 rpm twice to remove the unexfoliated graphite. The concentration of the GO solution was assessed through filtration, drying, and weighing of the GO film.

### S2. Determination of Dose Rate through Fricke Dosimetry

Fricke dosimetry is a reliable technique for quantifying the radiation dose rate of γ-radiation. When ionizing radiation interacts with a specific medium, it triggers a chemical reaction that can be quantified to ascertain the absorbed dose. The Fricke solution, based on this principle, comprises a blend of $FeSO_4$, $H_2SO_4$, and NaCl. This solution is divided into 5 identical vials of equal volume and concentration, each labeled accordingly. Subsequently, these vials are subjected to irradiation within a $^{60}Co$ chamber. At appropriate intervals, samples from each vials are extracted, and UV spectra are recorded to gauge the alteration in absorbance of $Fe^{3+}$ at 304 nm. A graph is then plotted correlating absorbance with time to derive the slope, and calculations are performed utilizing the equation (1):

$$D = \frac{0.967\ x\ 10^7 x\ slope}{\varepsilon b \rho G(product)} \qquad (1)$$

where $\varepsilon$ is the molar absorption coefficient of $Fe^{3+}$ (2174 $dm^3\ mol^{-1}\ cm^{-1}$), b is the path length and $\rho$ is the density of the Fricke solution. To obtain G(product), we need to consider the

primary species produced during the radiolysis of water with the Fricke solution as described below:

$H_2O \rightarrow e^-_{aq} + H^+$, $H_3O^-$, $H^\cdot$, $OH^\cdot$, $H_2$, $H_2O_2$

$H^\cdot + OH^\cdot \rightarrow HO_2^\cdot$

$HO_2^\cdot + Fe^{3+} \rightarrow HO_2^- + Fe^{3+}$

$HO_2^- + H^+ \rightarrow H_2O_2$

$H_2O_2 + Fe^{2+} \rightarrow OH^\cdot + OH^- + Fe^{3+}$

$OH^\cdot + Fe^{2+} \rightarrow OH^- + Fe^{3+}$

Thus, the final product of this reaction is $Fe^{3+}$ and its overall yield is

$G(Fe^{3+}) = 3G(H^\cdot) + 2G(H_2O_2) + G(OH^\cdot) = 15.5$

Using these calculations, the dose rate was determined to be 15 Gy $min^{-1}$.

## S3. Material Characterization

The X-ray absorption spectroscopy experiments, including both X-ray absorption near edge structure (XANES) and extended X-ray absorption fine structure (EXAFS), were performed on the scanning EXAFS beamline (BL-09) at Indus-2 SRS, Raja Ramanna Centre for Advanced Technology (RRCAT), Indore, India. The beamline was furnished with a double-crystal monochromator utilizing Si (111) crystals for energy selection and a meridional cylindrical mirror coated with Rh and Pt for collimation. The measurements were executed at room temperature and employed transmission mode. $N_2$, He and Ar gases were introduced into the ion chambers for both the Pt foil and the samples for accurate measurements. The XANES and EXAFS measurements were executed utilizing the quick-X-ray absorption spectroscopy (XAS) mode, which employs a continuous scan over the energy or angle range, deviating from the conventional step-by-step scanning employed during XAS data acquisition. To suppress the higher harmonic components, the second crystal of the monochromator was deliberately set to a 60% detuned state during the data collection. The energy calibration was performed using Pt metal foil at 11564 eV as a reference. The standard normalization and background subtraction procedures were executed using the ATHENA software version 0.9.26 to obtain normalized XANES spectra [2]. Fourier transformed (FT) EXAFS oscillations were calculated to observe the $|\chi(R)|$ *vs* $R$ space spectra and its fitting was done using ARTEMIS software version 0.9.26 which uses FEFF6 and ATOMS[2] programs to simulate the theoretical scattering paths according to crystallographic structure [3].

## S4. Electrochemical Characterization

All the electrochemical experiments were carried out using a three-electrode cell at room temperature with a Bio-Logic SAS (VSP-300) electrochemical workstation. To investigate all the electrochemical processes, a glassy carbon rotating disk electrode (RDE) with diameter 4 mm, graphite rod, and Ag/AgCl electrode were used as the working, counter, and reference electrode, respectively. For ORR (Oxygen Reduction Reaction), an additional setup, Rotating Ring Disc Electrode (RRDE) setup was employed, comprising a glassy carbon electrode alongside a platinum ring. The RRDE setup featured a collection factor of 0.35, and the relevant measurements are detailed in S8 and S9. The catalyst ink was prepared by mixing 5 mg of the catalyst in 1 ml of stock solution (consisting of 100 µl of Nafion solution, 5 ml of isopropanol, and 20 ml of Milli-Q water) under vigorous ultrasonic treatment for 30 min. Subsequently, 6 µL of the obtained catalyst ink was loaded onto the electrode. All the measured potentials in electrochemical experiments were converted to reversible hydrogen electrode (RHE) by the conversion factor $E_{RHE} = E^{o} + E_{Ag/AgCl} + 0.0591pH$.

In ORR, the CV measurements were performed in $N_2$-saturated 0.1 M $HClO_4$ solutions at a scan rate of 100 mV $s^{-1}$. LSV measurements were performed at a scan rate of 10 mV $s^{-1}$ at different rotations from 400 to 2500 rpm. The electrochemical active surface area (ECSA) of the catalysts was determined from the hydrogen underpotential deposition (HUPD) region within the potential range of 0.05-0.35 V, assuming a double layer correction of 210 µC $cm^{-2}$ corresponding to the adsorption of a hydrogen monolayer in an acidic electrolyte (details given in S5). The specific activity (SA) and mass activity (MA) (details given in S6) of the catalysts were computed by normalizing the kinetic current density with respect to the electrochemical surface area and the loading amount of Pt metal. To assess the stability of the catalyst for ORR, polarization curves were obtained before and after subjecting the system to 10,000 cycles in $O_2$-saturated solutions. Detailed information regarding all parameters computed for ORR is provided in S5-S10 of the supporting information.

For OER and HER, the LSV curves were generated at a scan rate of 10 mV $s^{-1}$ in $N_2$-saturated 0.1 M $HClO_4$. All kinetic measurements were benchmarked against 10 wt% Pt/C on Vulcan XC72 carbon.

## S5. Determination of Electrochemical Active Surface Area (ECSA) for ORR

The electrochemical active surface area (ECSA) of the catalysts was calculated from the Hydrogen underpotential deposition ($H_{upd}$) region in the potential range of 0.05-0.35 V after assuming the double layer correction of 210 μC $cm^{-2}$, corresponding to the adsorption of hydrogen monolayer in acidic electrolyte. The value of the ECSA was calculated from the equation 2:

$$ECSA = \frac{Q_{H-adsorption}(C)}{210\left(\frac{\mu C}{cm_{Pt}^2}\right) L_{Pt}\left(\frac{mg_{Pt}}{cm^2}\right) A_g(cm^2)} 10^5 \qquad (2)$$

where $Q_{H\text{-adsorption}}$ (C) is the charge of hydrogen adsorption/desorption. The charge associated with full monolayer coverage on a clean polycrystalline Pt is $Q_H$ = 210 μC $cm_{Pt}^{-2}$ and is used as a conversion factor. The Pt loading on the glassy carbon electrode, $L_{Pt}$ calculated from ICP-MS values and reported in $mg_{Pt}$ $cm^{-2}$, while $A_g$ is the surface area of glassy carbon electrode (i.e. 0.126 $cm^2$) [4][5][6].

## S6. Determination of Specific Activity (SA) and Mass Activity (MA) for ORR

The SA and MA of the catalysts were calculated after normalizing the kinetic current density ($j_k$) by ECSA and loading amount of Pt metal using the equations (3-4) [5][7].

$$MA\ (mA/\mu g_{Pt}) = \frac{j_k}{Pt\ loading} \qquad (3)$$

$$SA\ (mA/cm^2) = \frac{j_k}{ECSA} \qquad (4)$$

## S7. Determination of n-value using K-L Plot for the ORR

The ORR kinetics analysis can be conducted using Koutecky-Levich (K-L) equation. It is derived from the principles of mass transport and kinetics in electrochemical systems and is given by the equation (5 and 6) [6][7]:

$$\frac{1}{j} = \frac{1}{j_d} + \frac{1}{j_k} = \frac{1}{B\sqrt{w}} + \frac{1}{j_k} \qquad (5)$$

$$B = 0.62nF D^{2/3} \upsilon^{-1/6} C_o \qquad (6)$$

where ω is the angular velocity, υ is kinematic viscosity of the electrolyte ($1.009 \times 10^{-2}$ $cm^2$ $s^{-1}$ ) in 0.1M $HClO_4$ , n is the overall number of electron transferred in the ORR, F is the Faraday constant (96 500 C $mol^{-1}$), $C_o$ is the $O_2$ saturated concentration in the 0.1 M $HClO_4$

electrolyte (1.26 x $10^{-3}$ mol $L^{-1}$), D is the diffusion coefficient of oxygen in the 0.1 M $HClO_4$ electrolyte (1.93 x $10^{-5}$ $cm^2$ $s^{-1}$) [7].

K-L plots obtained from the LSV curves ($j^{-1}$ vs. $\omega^{-1/2}$) were analyzed at various electrode potentials. The slopes were used to calculate the transferred electron number (n) per oxygen molecule involved in the ORR on the basis of the K-L equation. The n value provides information about the number of electrons transferred in the electrochemical reaction

## S8. Calculation of n and p values using RRDE for ORR

The rotating ring disk electrode (RRDE) was also utilized to study kinetics and mechanism of ORR. It consists of a glassy carbon electrode and platinum ring. For RRDE study, the ink and electrode were prepared using similar method as that of RDE; with only difference of catalyst loading (6 µl on the 4 mm diameter). The RRDE characterization was performed in the potential range between -0.2 V to 1.0 V vs Ag/AgCl with sweep rate 10 $mVs^{-1}$ from 400 to 2500 rpm and the ring held at constant potential 1 V (vs Ag/AgCl). The amount of peroxide intermediate (% yield of $H_2O_2$) and number of electron transfer (n) were calculated using following equations (7) and (8).

$$n = 4\frac{i_d + \frac{i_r}{N}}{\frac{j_r}{N}} \qquad (7)$$

$$HO_2^- = \frac{200\, x\, \frac{i_r}{N}}{i_d + \frac{i_r}{N}} \qquad (8)$$

where, $i_d$ is the disk current, $i_r$ is ring current and N = 0.35 is collection efficiency of Pt ring in this experiment (procedure to determine collection efficiency is given below).

## S9. Determination of Collection Efficiency (N) for ORR

The calibration of the collection efficiency (N) of RRDE is necessary prior to any collection experiments. To determine N, a redox solution containing a known concentration of electroactive species is chosen so that it could be electrochemically oxidized or reduced at the disk [8][9]. Here, 2mM $K_3Fe(CN)_6$ solution was prepared in 0.1M $KNO_3$ solution to be used as the electrolyte. The RRDE electrodes were dipped into this $N_2$-saturated solution and potential was scanned between 0.6 V to -0.2 V vs Ag/AgCl by the disk electrode while the

ring electrode was fixated at 0.6 V to drive the electrode reaction. Both the currents generated at the disk and ring electrodes during the calibration experiment were recorded at various rotation rates. The reactions taking place at the disk and ring electrodes being $Fe(CN)_6^{3-} + e^- \rightarrow Fe(CN)_6^{4-}$ and $Fe(CN)_6^{4-} \rightarrow Fe(CN)_6^{3-} + e^-$, respectively. The i-V curves obtained are assessed to get the N value by the equation (9),

$$N = \frac{|i_{r,l}|}{|i_{d,l}|} \qquad (9)$$

The collection efficiency was obtained to be 0.35. In addition, we also determined its value theoretically and it was found to be 0.4. This difference can be attributed to the electrode geometry which may have imperfections and also to the negligence of mass-transport limitations in the theoretical calculations [8][9].

## S10. Calculation of Tafel Slope for ORR, OER and HER

The Tafel plots was obtained from the polarization curves by plotting the overpotential (η) *vs* logarithm of the absolute value of current density (|j|) using the equation (10 and 11) in case of ORR, OER and HER:

$$\eta = \frac{2.303RT}{\alpha nF}\log j_0 - \frac{2.303RT}{\alpha nF}\log j_k \qquad (10)$$

$$\eta = b\ log\ j_0 + c \qquad (11)$$

where η (mV) indicates the applied overpotential, α is the transfer coefficient, and $j_k$, $j_o$ (mA $cm^{-2}$) are the kinetic and exchange current densities respectively, b (mV $dec^{-1}$) is the Tafel slope.

## S11. Calculation of Turnover Frequency (TOF) of HER

TOF calculation [10][11]: The TOF per metal (Pt-based) site in the developed catalyst for the HER is calculated by the equation (12):

$$TOF = \frac{Total\ number\ of\ hydrogen\ turnover/\ geometric\ area\ (cm^2)}{Number\ of\ active\ sites\ /\ geometric\ area\ (cm^2)} \qquad (12)$$

The total number of hydrogen turnovers was calculated from the current density (at η = -20mV) using the equation (13):

$$Total\ no{:}\ of\ H_2 = \left(j\frac{mA}{cm^2}\right)\left(\frac{1C/s}{1000mA}\right)\left(\frac{1\ mol\ e^-}{96485.3\ C}\right)\left(\frac{1\ mol\ H_2}{2\ mol\ e^-}\right)\left(\frac{6.02 \times 10^{23}\ molecules}{1\ mol\ H_2}\right.$$

From the ICP-MS measurement, the Pt loading was determined and shown in Table S4. Thus the number of active site density (NAS) based on bulk Pt is obtained by the equation (14) and shown in Table 7:

$$NAS = Pt\ (wt\%)\ x\ Pt\ loading\ on\ GCE\ \left(mg\ cm^{-2}\right) \times \frac{1\ mM}{195.1(mg)} \times 6.0 \quad (14)$$

Thus, per-site turnover frequency (TOF) of the catalyst is determined from equation (15),

$$TOF = \frac{Total\ no{:}\ of\ H_2\ x\ 10\ mA\ cm^{-2}}{NAS} \quad (15)$$

## S12. Calculation of Work Function (ϕ) using the Retarding Field Method

The work function (ϕ) of $Ti_3C_2T_x$-rGO support was determined using the retarding field method (modified diode method) . For this purpose, a low-energy (10 eV) electron gun with magnetic focusing was employed. The electron current directed at the sample was reduced by applying a time-varying negative potential relative to the cathode. Generally, the target current as a function of the retarding field is described in the equation 16 and 17:

$$I_t = AT_c^2\ exp[\frac{\left(eV_t - e\emptyset_t\right)}{kT_c}] \quad (16)$$

$$ln\left(I_t\right) = \ln AT_c^2 + \frac{e}{kT_c}\left(V_t - \emptyset_t\right) \quad (17)$$

where, A is a constant and $T_c$ is the cathode temperature. In diode method the target current is a monotonic function of the retarding potential $V_t$ given in equation 18:

$$I_t = f\left(\emptyset_t - V_t\right) \quad (18)$$

In this setup, $V_t$ represents the potential difference between the cathode of the electron gun and the target, while $\phi_t$ denotes the work function of the target. The incident electron current on the sample was recorded using a Keithley 2400 multimeter as a function of the retarding potential. When plotting the sample current (on a logarithmic scale) against the applied retarding potentials, the resulting straight line provides the necessary information. Gold was

used as a reference sample, and the shift on the X-axis ($V_t$ axis) for the sample relative to gold was used to determine the work function of the sample under investigation.

---

## II. LIST OF FIGURES

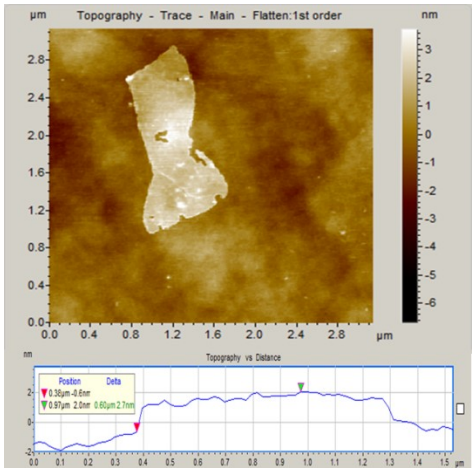


***Figure S1:*** *AFM image of $Ti_3C_2T_x$ MXene nanosheets and its related analysis file shown below.*

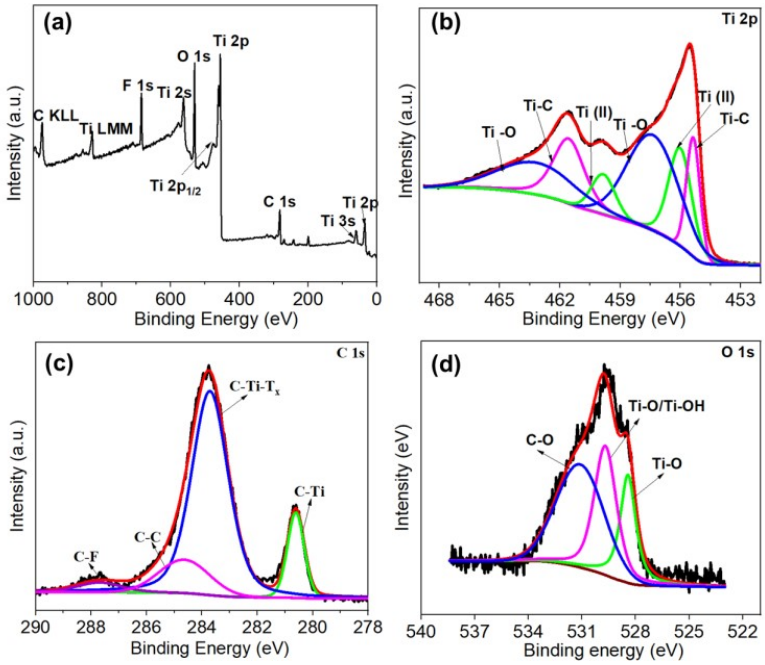


***Figure S2:*** *(a) XPS survey spectrum of $Ti_3C_2T_X$ MXene. High-resolution XPS spectra of (b) Ti2p, (c) C 1s, and (d) O 1s.*

The survey spectrum revealed distinct signals from Ti, C, O, and F (Figure S2a). Peaks at binding energies of 33, 120, 284, 453, 476, 530, 557, 682, 832, and 985 eV correspond to Ti 2p, Ti 3s, C 1s, Ti 2p, Ti $2p_{1/2}$, O 1s, Ti 2s, F 1s, Ti LMM, and C KLL, respectively [12][13][14]. The high-resolution Ti 2p spectra (Figure S2b) show three doublets at 454.05 (460.5), 455.25 (458.2), and 456.8 (464.15) eV, attributed to Ti-C, Ti-O, and Ti-X, respectively. The C 1s spectra (Figure S2c) are deconvoluted into four peaks, indicating C-Ti (280.9 eV), C-Ti-Tx (283.75 eV), C-C (284.6 eV), and C-F (287.75 eV). The O 1s spectra (Figure S2d) show three peaks, including one at 532.35 eV due to the C-O bond, with the others at 529.4 and 531.05 eV assigned to O bound to Ti. These XPS findings align with previous reports on $Ti_3C_2T_x$ MXene, confirming its successful preparation [12][13].

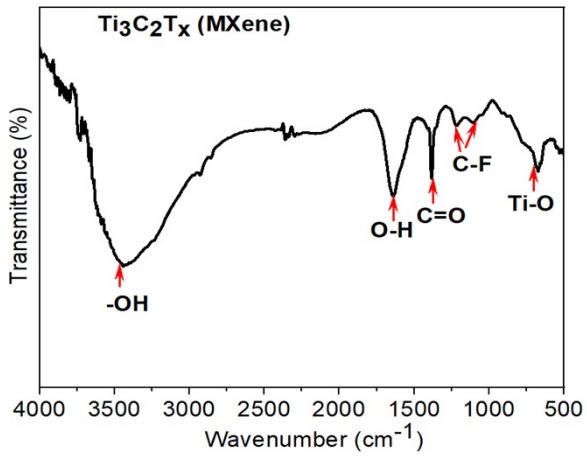


***Figure S3:*** *FTIR spectrum of $Ti_3C_2T_X$ MXene.*

The FTIR spectrum (Figure S3) of $Ti_3C_2T_x$ shows a broad band around 3450 $cm^{-1}$, assigned to O-H stretching vibrations. The broad nature of the band suggests extensive hydrogen bonding. At 1637 $cm^{-1}$, the spectrum exhibits a band corresponding to C=O stretching vibrations, associated with the presence of carbonyl groups (C=O) formed during the synthesis or post-treatment of $Ti_3C_2T_x$, indicating oxidation on the surface. A band at 1378 $cm^{-1}$ is assigned to O-H bending vibrations, reinforcing the presence of hydroxyl functionalities on the surface of the $Ti_3C_2T_x$. The band at 1104 $cm^{-1}$ is attributed to C–F stretching vibrations. The peak at 668 $cm^{-1}$ is associated with Ti–O stretching vibrations, suggesting the presence of Ti-O bonds due to partial oxidation of the titanium layers within the $Ti_3C_2T_x$ structure [15][16].

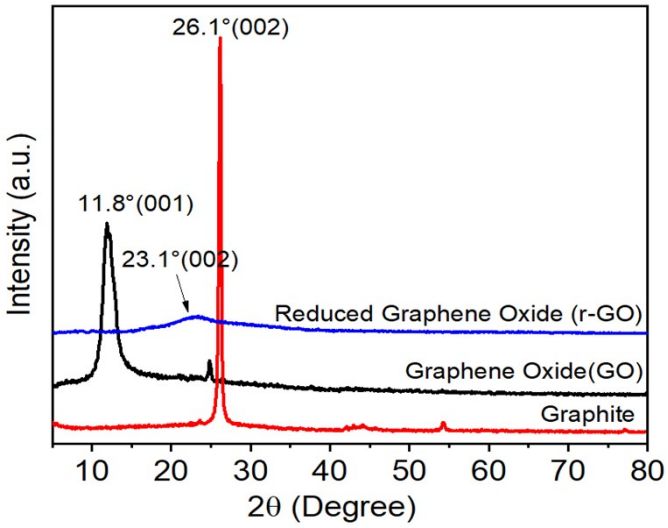


***Figure S4:*** *(a) XRD patterns of graphite, GO, and rGO (obtained after radiolysis).*

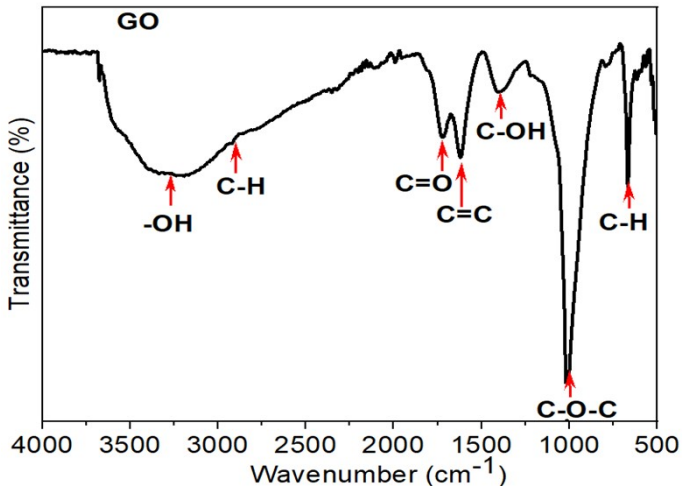


***Figure S5:*** *(a) FTIR spectrum of GO nanosheets.*

The FTIR analysis of GO (Figure R3b) reveals a broad band around 3400 $cm^{-1}$ (O-H stretching, indicating hydroxyl groups and adsorbed water), a band at ~1730 $cm^{-1}$ (C=O stretching from carbonyl groups, highlighting oxidation), a band near 1620 $cm^{-1}$ (C=C stretching, reflecting residual aromatic structure), a band around 1380 $cm^{-1}$ (O-H bending and/or C-O stretching, representing hydroxyl and epoxide groups), band at 1080 $cm^{-1}$ (C-O stretching from C-O-C groups), and a band at ~ 670 $cm^{-1}$ (C-H bending vibrations) [15][16].

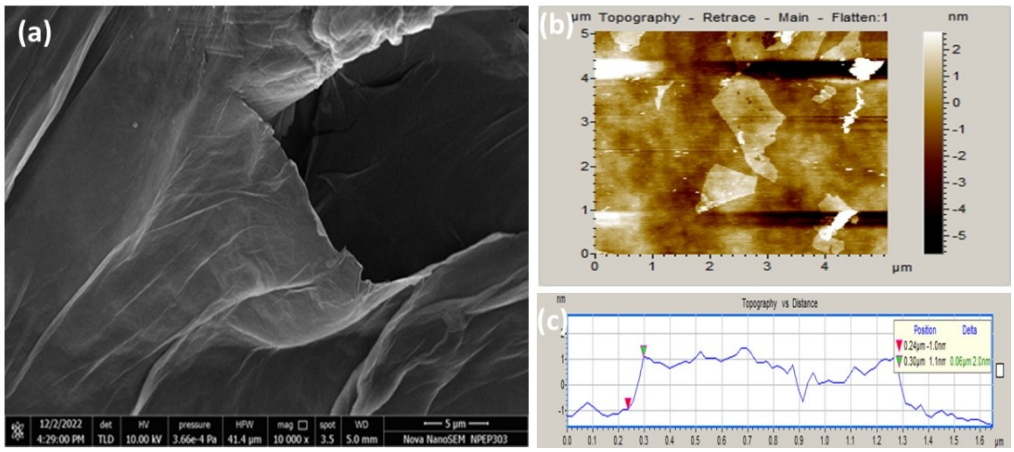


***Figure S6:*** *(a ) SEM image of GO nanosheets. (b and c) AFM images of GO nanosheets and its related analysis profile.*

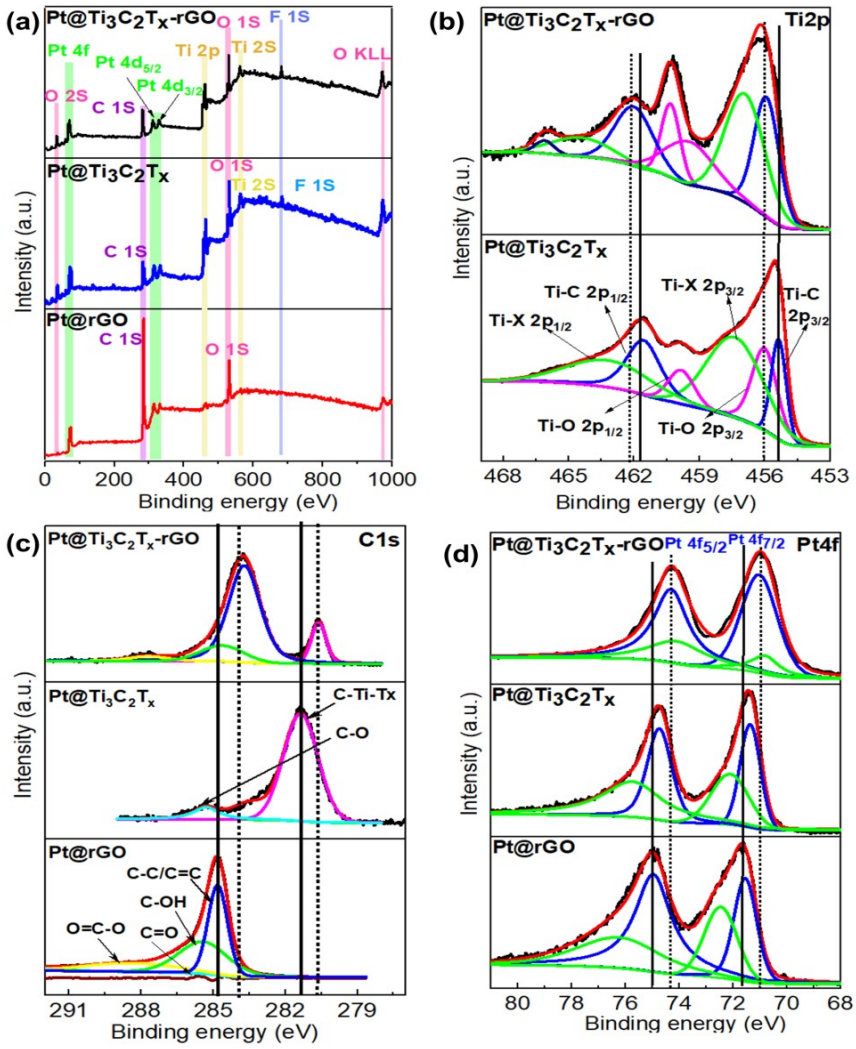


***Figure S7.*** *(a) XPS survey spectrum of Pt@$Ti_3C_2T_x$-rGO, Pt@$Ti_3C_2T_x$, and Pt@rGO. High-resolution XPS spectra of (b) Ti 2p, (c) C 1s, and (d) Pt 4f of Pt@$Ti_3C_2T_x$-rGO, Pt@$Ti_3C_2T_x$, and Pt@rGO.*

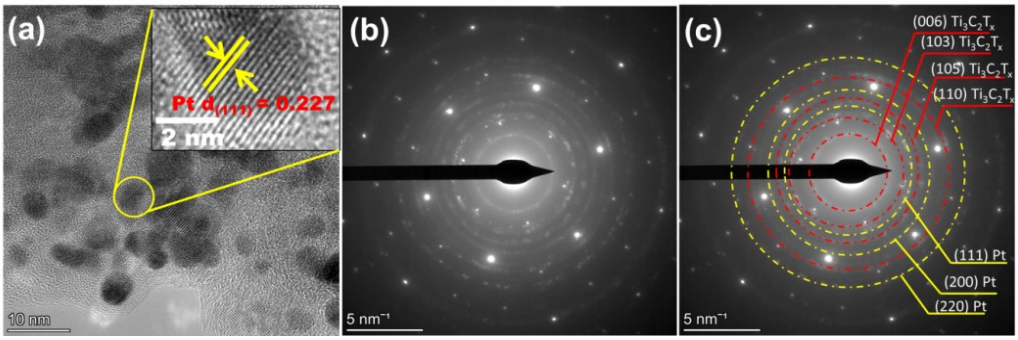


***Figure S8:*** *(a) TEM image of Pt@$Ti_3C_2T_x$-rGO aerogel (inset shows high resolution TEM (HR-TEM) image of Pt over Pt@$Ti_3C_2T_x$-rGO.) (b and c) selected area electron diffraction (SAED) pattern of Pt@$Ti_3C_2T_x$-rGO (non-indexed and indexed images, respectively).*

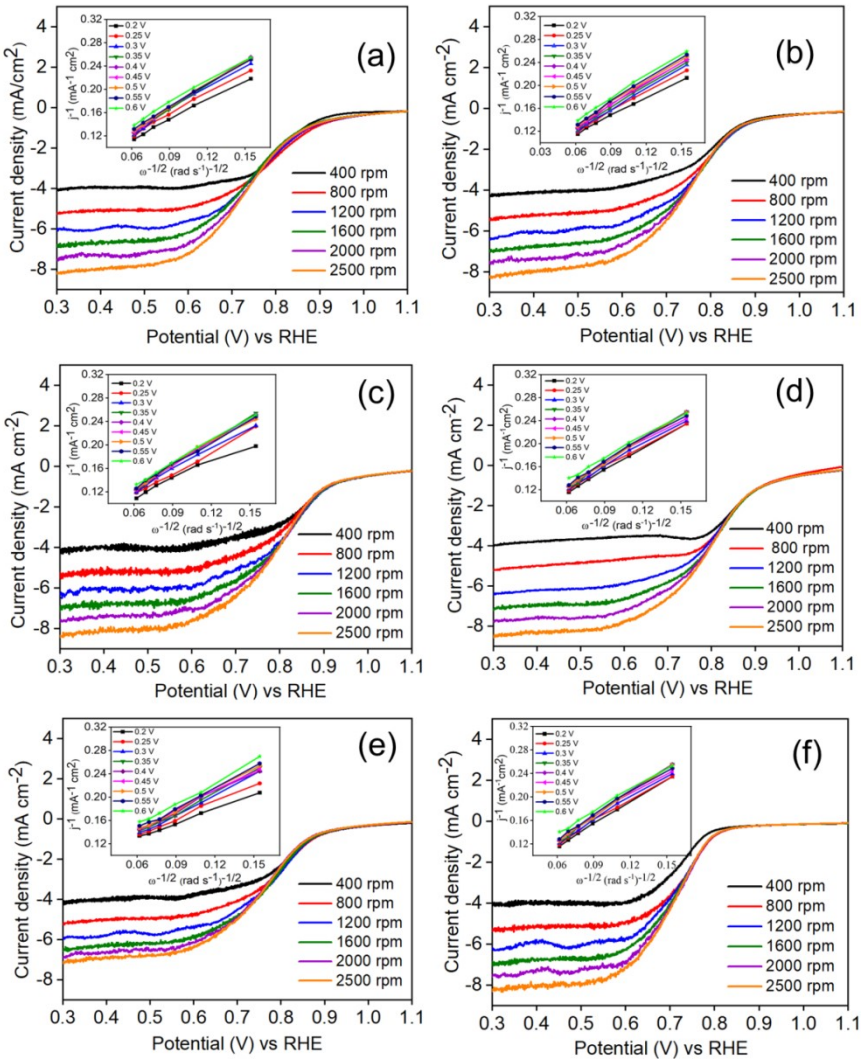


.

***Figure S9**: LSV curves of (a) Pt@$Ti_3C_2T_x$-rGO 1:3, (b) Pt@$Ti_3C_2T_x$-rGO 1:1, (c) Pt@$Ti_3C_2T_x$-rGO 3:1, (d) Pt@$Ti_3C_2T_x$, (e) Pt@r-GO, and (f) Pt/C catalysts obtained in an $O_2$-saturated 0.1 M $HClO_4$ electrolyte with different rotating rates (corresponding Koutecky-Levich (K-L) plots of catalysts at different potentials are shown in the inset).*

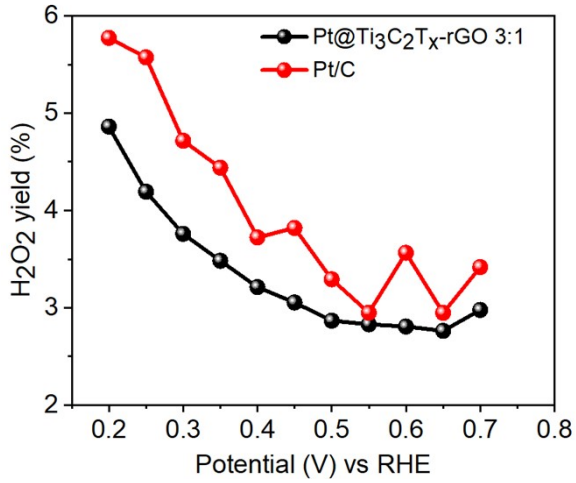


***Figure S10.** Percentage peroxide yield in Pt@$Ti_3C_2T_x$-rGO 3:1 and Pt/C.*

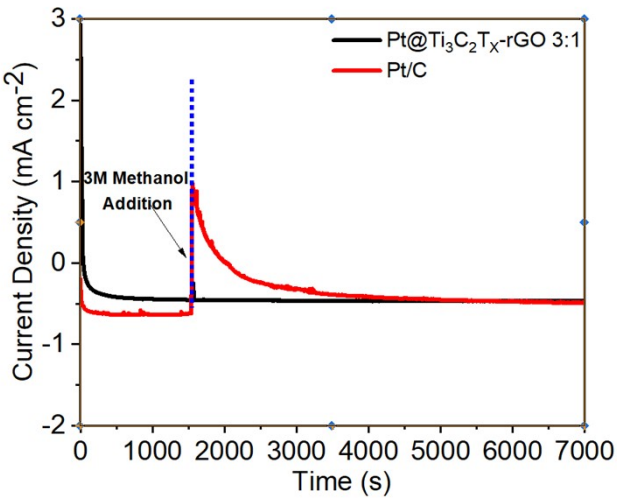


***Figure S11:*** *Current-time (i-t) chronoamperometric response of $Pt@Ti_3C_2T_x$-rGO 3:1 and Pt/C by adding 3 M methanol after 1500 s at −0.4 V in $O_2$-saturated 0.1 M $HClO_4$.*

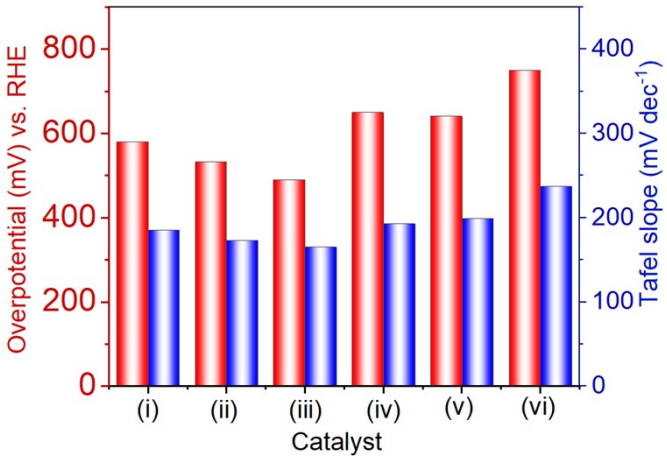


***Figure S12:*** *Comparison of OER catalytic performance (overpotential and Tafel slope values) of (i) $Pt@Ti_3C_2T_x$-rGO 1:3, (ii) $Pt@Ti_3C_2T_x$-rGO 1:1, (iii) $Pt@Ti_3C_2T_x$-rGO 3:1, (iv) $Pt@Ti_3C_2T_x$, (v) Pt@r-GO, and (vi) Pt/C catalysts.*

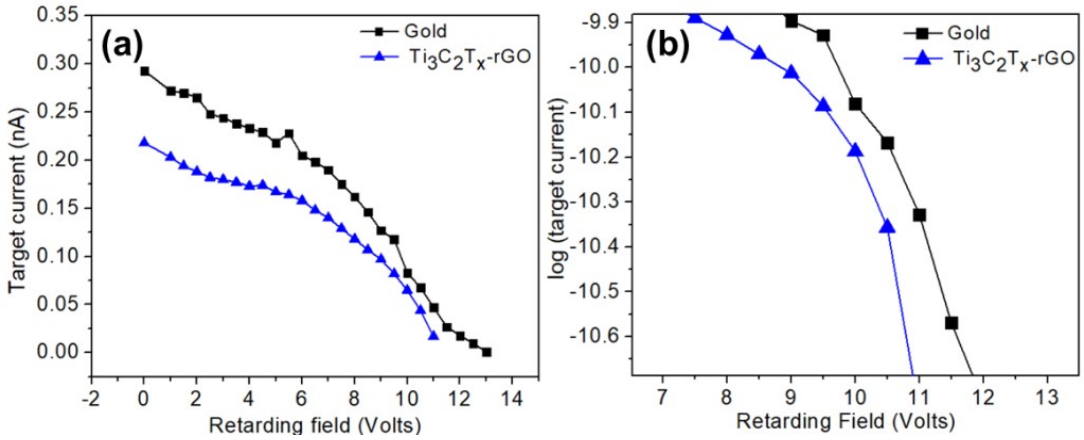


***Figure S13****: Shows the target current vs Retarding potential curve (b) Shows logarithmic*

*plots of target current vs retarding potential for $Ti_3C_2T_x$-rGO support and gold as reference.*

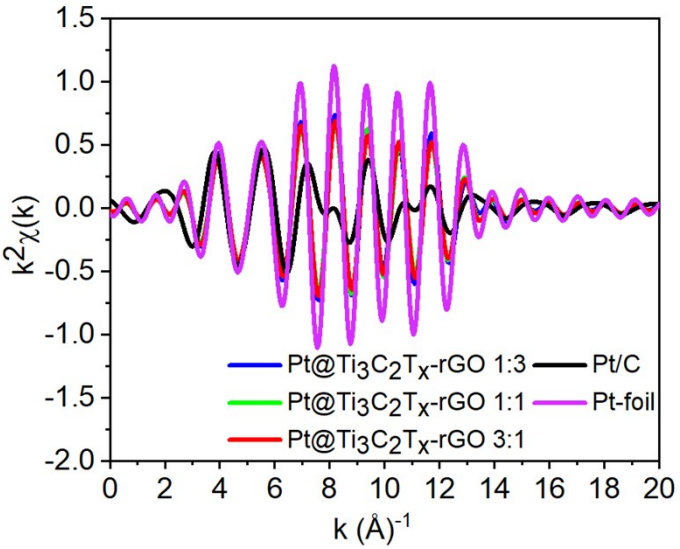


***Figure S14.*** *EXAFS k-space spectra* $k^2$-weighted Pt $L_3$-edge EXAFS spectra

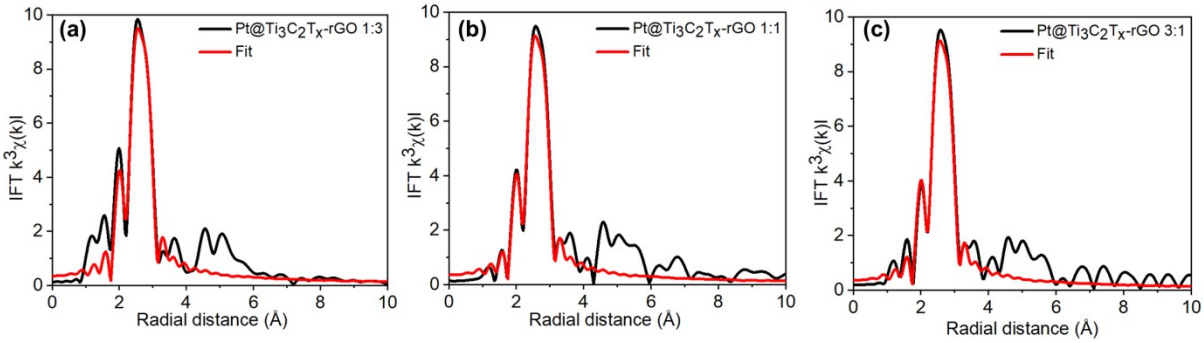


***Figure S15.*** *Quantitative fitting of Fourier-transformed EXAFS (FT-EXAFS) in R space for (a) Pt@$Ti_3C_2T_x$-rGO 1:3, (b) Pt@$Ti_3C_2T_x$-rGO 1:1 and (c) Pt@$Ti_3C_2T_x$-rGO 3:1*

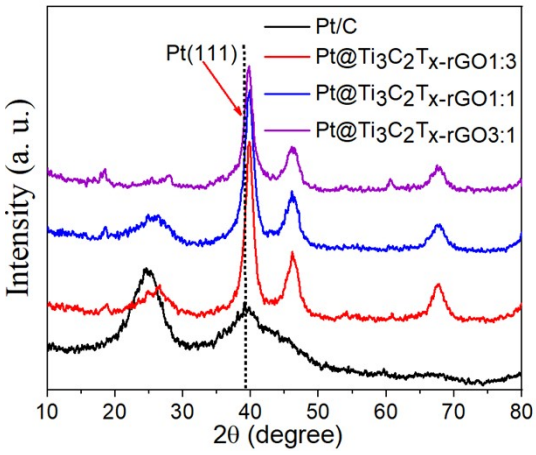

***Figure S16:*** *XRD patterns of Pt@$Ti_3C_2T_x$-rGO 1:3, Pt@$Ti_3C_2T_x$-rGO 1:1 and (c) Pt@$Ti_3C_2T_x$-rGO 3:1 and Pt/C catalysts (dotted line showing the higher angle shift of Pt (111) plane in Pt@$Ti_3C_2T_x$-rGO catalysts compared to Pt/C)*

---

## III LIST OF TABLES

**Table S1:** Summary of the $d_{(200)}$ XRD peaks of bulk $Ti_3AlC_2$, exfoliated and delaminated $Ti_3C_2T_x$ MXene.

| Samples | Average crystallite Size (D) (nm) | 2θ (°) of $d_{(002)}$ | d-spacing of $d_{(002)}$ |
|---|---|---|---|
| Bulk $Ti_3AlC_2$ | 32.7 | 9.6 | 0.930 |
| Exfoliated $Ti_3C_2T_x$ MXene | 11.2 | 8.7 | 1.036 |
| Delaminated $Ti_3C_2T_x$ MXene | 6.69 | 6.9 | 1.334 |

**Table S2:** Summary of the $d_{(002)}$ and $d_{(001)}$ XRD peaks of graphite, graphene oxide (GO) and reduced graphene oxide (rGO obtained after radiolysis)

| Samples | 2θ (°) | d-spacing (nm) | Average crystallite Size (D) (Å) |
|---|---|---|---|
| Graphite | 26.1 of $d_{(002)}$ | 0.342 | 3.36 |
| Graphene Oxide(GO) | 11.8 of $d_{(001)}$ | 0.881 | 6.57 |
| Reduced Graphene Oxide(r-GO) | 23.1 of $d_{(002)}$ | 0.401 | 3.89 |

**Table S3:** Summary of texture parameters of the all the catalysts from $N_2$ adsorption-desorption physisorption analysis.

| Sample | $S_{BET}$ [a] ($m^2\ g^{-1}$) | Pore volume [b] ($cm^3\ g^{-1}$) | Pore size distribiution (nm) |
|---|---|---|---|
| Pt@$Ti_3C_2T_x$-rGO 1:3 | 125.32 | 0.123 | 4.756 |
| Pt@$Ti_3C_2T_x$-rGO 1:1 | 111.23 | 0.103 | 7.62 |
| Pt@$Ti_3C_2T_x$-rGO 3:1 | 101.21 | 0.098 | 8.29 |
| Pt@$Ti_3C_2T_x$ | 48.69 | 0.069 | 12.58 |
| Pt@rGO | 110.63 | 0.156 | 4.85 |
| $Ti_3C_2T_x$ | 13.23 | 0.035 | 12.35 |
| r-GO | 96.56 | 0.108 | 3.74 |

*[a] The specific surface area was calculated by the Brunauer-Emmett-Teller ($S_{BET}$) method. $S_{BET}$ calculated in the region of $P/P_0$ =0.05 to 0.3. [b] Pore volume represents the total pore volume, determined at $P/P_0$=0.9997.*

**Table S4**: Percentage of Pt-loading of the developed catalysts determined from ICP-MS measurements.

| Sample | Total Pt loading (%) |
|---|---|
| Pt@$Ti_3C_2T_x$-rGO 1:3 | 7.14 |
| Pt@$Ti_3C_2T_x$-rGO 1:1 | 7.16 |
| Pt@$Ti_3C_2T_x$-rGO 3:1 | 9.74 |
| Pt@$Ti_3C_2T_x$ | 8.93 |
| Pt@rGO | 8.91 |
| Pt/C (standard) | 10 |

**Table S5.** Summary of the integrated area of XRD peaks of (111) and (200) plane.

| Catalyst | Integrated Area of (111) | Integrated Area of (200) | Volume fraction of (100) |
|---|---|---|---|
| Pt@$Ti_3C_2T_x$-rGO (1:3) | 1488.23 | 633.68 | 2.34 |
| Pt@$Ti_3C_2T_x$-rGO (1:1) | 2615.15 | 1036.33 | 2.52 |
| Pt@$Ti_3C_2T_x$-rGO (3:1) | 2809.16 | 917.72 | 3.06 |
| Pt@$Ti_3C_2T_x$ | 1855.60 | 743.65 | 2.49 |
| Pt@rGO | 3865.09 | 1347.77 | 2.86 |

**Table S6:** Summary of the electrochemical properties for ORR of the catalysts in $O_2$-saturated 0.1 M $HClO_4$ electrolyte. (All data were taken from the LSV tests at a rotational speed of 1600 rpm).

| Sample | ECSA ($m^2\ g^{-1}$) | [a]$E_{onset}$ (V) | [b]$E_{1/2}$ (V) | [c]$j_d$ (mA $cm^{-2}$) | [d]MA (mA $\mu g_{Pt}^{-1}$) | [e]SA (mA $cm^{-2}$) | Tafel Slope (mV $dec^{-1}$) |
|---|---|---|---|---|---|---|---|
| Pt@$Ti_3C_2T_x$-rGO 1:3 | 50.32 | 0.918 | 0.772 | -6.50 | 0.048 | 0.096 | -120.80 |
| Pt@$Ti_3C_2T_x$-rGO 1:1 | 48.31 | 0.925 | 0.793 | -6.58 | 0.069 | 0.144 | -115.07 |
| Pt@$Ti_3C_2T_x$-rGO 3:1 | 80.12 | 0.957 | 0.813 | -6.98 | 0.132 | 0.146 | -112.77 |
| Pt@$Ti_3C_2T_x$ | 75.67 | 0.925 | 0.801 | -6.85 | 0.097 | 0.128 | -114.45 |
| Pt@rGO | 59.77 | 0.872 | 0.737 | -6.13 | 0.043 | 0.046 | -123.30 |
| Pt/C (10%) | 56.13 | 0.885 | 0.763 | -6.83 | 0.021 | 0.097 | -121.39 |

[a] Half-Wave Potential, [b] onset –potential, [c] current density, [d] mass activity, [e] specific activity

**Table S7:** Total number of hydrogen turnovers and active site density based on bulk Pt of the investigated catalyst

| Samples | Total number of hydrogen turnovers ( $H_2\ s^{-1}\ cm^{-2}$ per mA $cm^{-2}$) | No: Active site (NAS) ( $s^{-1}$ per Pt sites) | turnover frequency (TOF) per Pt sites |
|---|---|---|---|
| Pt@$Ti_3C_2T_x$-rGO 1:3 | $8.71 \times 10^{15}$ | $6.92 \times 10^{15}$ | 12.58 |
| Pt@$Ti_3C_2T_x$-rGO 1:1 | $8.49 \times 10^{15}$ | $6.18 \times 10^{15}$ | 13.73 |
| Pt@$Ti_3C_2T_x$-rGO 3:1 | $14.47 \times 10^{15}$ | $11.42 \times 10^{15}$ | 12.67 |
| Pt@$Ti_3C_2T_x$ | $6.96 \times 10^{15}$ | $9.71 \times 10^{15}$ | 7.17 |
| Pt@rGO | $4.65 \times 10^{15}$ | $9.65 \times 10^{15}$ | 4.81 |
| Pt/C | $8.45 \times 10^{15}$ | $12.22 \times 10^{15}$ | 6.92 |

**Table S8**: Summary of ORR performance of MXene-based hybrid heterostructure

| Electrocatalyst | Synthesis Route | Electrolyte | Half-Wave Potential (V) | References |
|---|---|---|---|---|
| **Pt@$Ti_3C_2T_x$-rGO** | **Gamma-radiolysis** | **0.1 M $HClO_4$** | **0.828** | **Present Work** |
| Pt/TfGnP | Chemical Reduction | 0.1 M $HClO_4$ | 0.729 | 17 |
| Pt/$Nb_2O_5$/C | Chemical Reduction | 0.1 M $HClO_4$ | 0.787 | 18 |
| PtNW/PCNF | Ultrasonic Reduction | 0.5 M $H_2SO_4$ | 0.768 | 19 |
| Pt/MWCNT-400 | Reduction by Magnetron Sputtering | 0.05 M $H_2SO_4$ | 0.75 | 20 |
| Pt-Ir/MWCNT | Chemical Reduction by Refluxing | 0.1 M $HClO_4$ | 0.77 | 21 |
| Pt/CNT−$Ti_3C_2T_x$ | Self-Assembly Process | 0.1 M $HClO_4$ | 0.876 | 22 |
| N-doped graphene/ $Ti_3C_2T_x$ aerogel | Mechanical Mixing | 0.1 M KOH | 0.705 | 23 |
| Pt/$Ti_3C_2T_x$ | Ultrasonic Assisted Chemical Reduction | 0.5 M $H_2SO_4$ | 0.772 | 24 |
| Pt/MXene | Ultrasonic Assisted Chemical Reduction | 0.1 M $HClO_4$ | 0.766 | 25 |
| MXene@PPy-800 Heterostructure | In situ polymerization | 0.1 M KOH | 0.71 | 26 |
| Ru-SA/ $Ti_3C_2T_x$ | Ultrasonic assisted Freeze drying | 0.1 M $HClO_4$ | 0.80 | 27 |

| | | | | |
|---|---|---|---|---|
| $MoS_2$QDs@$Ti_3C_2T_x$QDs@ MWCNTs-2 Heterostructure | Thermal treatment | 1 M KOH | 0.75 | 28 |
| Fe-N-C@MXene Heterostructure | Thermal treatment in $N_2$ atmosphere | 0.1 M $HClO_4$ | 0.777 | 29 |
| $Pt_1$-N/BP | Refluxing followed by pyrolysis | 0.1 M $HClO_4$ | 0.76 | 30 |
| PdCu/C | Microwave reduction | 0.1 M $HClO_4$ | 0.73 | 31 |
| $Co_3O_4$/NCNTs/$Ti_3C_2$ Heterostructure | Pyrolysis | 0.1 M KOH | 0.79 | 32 |
| Pd@Ni-0.1/C Heterostructure | Ultrasonication followed by thermal reduction | 1 M KOH | 0.71 | 33 |
| PtPdRu/ nanodendrites Heterostructure | Reduction by continuous stirring | 0.1 M $HClO_4$ | 0.769 | 34 |
| g-$C_3N_4$/$Ti_3C_2$ Heterostructure | Thermal treatment in $N_2$ atmosphere | 0.1 M KOH | 0.79 | 35 |
| $MoS_2$/$Ti_3C_2T_x$/MMWCNT Heterostructure | Ultrasonication | 1.0 M KOH | 0.75 | 36 |

**Table S9:** Summary of HER performance of MXene-based hybrid heterostructure

| Electrocatalyst | Synthesis Route | Electrolyte | $\eta_{10mA/cm^2}$ (mV) | References |
|---|---|---|---|---|
| **Pt@$Ti_3C_2T_x$-rGO** | **Gamma-radiolysis** | **0.1 M $HClO_4$** | **43** | **Present Work** |
| MD$Ti_3C_2$/$MoS_x$-100 | Gamma-Radiolysis | 0.5 M $H_2SO_4$ | 165 | 37 |
| Pt/$Mo_2C$ | Atomic Layer Deposition | 0.5 M $H_2SO_4$ | 144 | 38 |
| Pt/TiWC | Reverse Microemulsion | 1 M $HClO_4$ | 100 | 39 |
| $Pt_1$@Fe-N-C | Incipient Wet Impregnation | 0.5 M $H_2SO_4$ | 60 | 40 |
| Pt/MWCNT | Potentiodynamic Method | 0.5 M $H_2SO_4$ | 84 | 41 |
| PPy($CoS_2$)MWCNTsPt | In-situ Electro-Polymerization | 0.5 M $H_2SO_4$ | 200 | 42 |
| Pd-$MoS_2$/MWCNT | Wet-Chemical Synthesis | 0.5 M $H_2SO_4$ | 120 | 43 |
| TBA-$Ti_3C_2T_x$-Pt-20 Heterostructure | Wet-Impregnation And Photoinduced Reduction | 0.5 M $H_2SO_4$ | 55 | 44 |
| N-$Ti_2CT_x$ Heterostructure | Nitridation Method | 0.5 M $H_2SO_4$ | 215 | 45 |
| $Ni_2P$/$Ti_3C_2T_x$/NF | Wet-Impregnation | 1 M KOH | 135 | 46 |
| N-$Ti_3C_2T_x$ Heterostructure | Ammonia Heat Treatment | 0.5 M $H_2SO_4$ | 198 | 47 |
| $Ti_3C_2T_x$@ rGO Heterostructure | Hydrothermal Method | 1 M KOH | 121 | 48 |
| Rh-Co-Ni LDH/$Ti_3C_2T_x$ | In-situ growth | 1 M KOH | 74.6 | 49 |
| LDH/MXene-RGO | Bottom-up approach | 1 M KOH | 326 | 50 |
| 40Pt-TBA-$Ti_3C_2T_x$ | Atomic layer deposition | 0.5 M $H_2SO_4$ | 67.8 | 51 |
| $Ti_3C_2T_x$@Pt/SWCNTs | Wet-Impregnation | 0.5 M $H_2SO_4$ | 62 | 52 |
| P-$Mo_2C$/$Ti_3C_2$@NC | polymerization and annealing | 0.5 M $H_2SO_4$ | 177 | 53 |
| PtNPs/$Ti_3C_2T_x$ | Chemical reduction | 0.1 M $H_2SO_4$ | 226 | 54 |
| $Ru_{SA}$-N-S-$Ti_3C_2T_x$ | Wet-Impregnation | 0.5 M $H_2SO_4$ | 76 | 55 |
| $Mo_2TiC_2T_x$-$Pt_{SA}$ | Electrochemical deposition | 0.5 M $H_2SO_4$ | 30 | 56 |
| $Ti_3C_2T_x$@0.1Pt | Electrophoretic deposition | 0.5 M $H_2SO_4$ | 43 | 57 |
| $Pt_{3.21}$Ni@$Ti_3C_2$ | Chemical reduction | 0.1 KOH | 55.6 | 58 |
| $MoS_2$/$Ti_3C_2$-MXene@C | Carbon-Nanoplating | 0.5 M $H_2SO_4$ | 135 | 59 |

**Table S10:** Relative intensity of Pt(0) and Pt(II) from XPS analysis

| Sample | Relative Intensity (wt.%) | |
|---|---|---|
| | Pt(0) | Pt(II) |
| Pt@$Ti_3C_2T_x$-rGO 1:3 | 68.72 | 31.29 |
| Pt@$Ti_3C_2T_x$-rGO 1:1 | 71.72 | 21.29 |
| Pt@$Ti_3C_2T_x$-rGO 3:1 | 86.56 | 29.34 |
| Pt/C (standard) | 56.85 | 43.15 |

**Table S11**: EXAFS fitting parameters

| Sample | N[a] | R (Å)[b] | $\sigma^2$ (Å)$^2$ [c] | $\Delta E_o$ (eV)[d] | r-factor (%)[e] |
|---|---|---|---|---|---|
| Pt@$Ti_3C_2T_x$-rGO 1:3 | 10.19 ± 1.085 | 2.750 | 0.00633 ± 0.000447 | 6.347 ± 0.575 | 0.006 |
| Pt@$Ti_3C_2T_x$-rGO 1:1 | 9.48 ± 0.542 | 2.748 | 0.00646 ± 0.000377 | 6.420 ± 0.910 | 0.005 |
| Pt@$Ti_3C_2T_x$-rGO 3:1 | 9.04 ± 0.625 | 2.730 | 0.00662 ± 0.000694 | 6.427 ± 0.486 | 0.018 |
| Pt foil | 12 | 2.771 | 0.00481 ± 0.00047 | 7.683 ±0.638 | 0.01 |

*[a]Coordination number [b]Bond distance [c]Debye-Waller factor [d]Difference in the threshold Fermi level between data and fit [e]goodness of fit parameter*

**Table S12**. Summary of XRD results regarding Pt(111) facets

| Catalysts | Lattice constant (Å) | Relative strain compared to Pt/C (%) |
|---|---|---|
| Pt@$Ti_3C_2T_x$-rGO | 3.9171 | 1.65 |
| Pt@$Ti_3C_2T_x$ | 3.9279 | 1.38 |
| Pt@rGO | 3.9237 | 1.49 |
| Pt/C | 3.9831 | 0 |

## REFERENCES


1. Ramesh, A.; Jeyavelan, M.; Leo Hudson, M. S. Electrochemical Properties of Reduced Graphene Oxide Derived through Camphor Assisted Combustion of Graphite Oxide. Dalt. Trans. **2018**, 47 (15), 5406–5414.
2. Ravel, B. ATOMS: Crystallography for the X-Ray Absorption Spectroscopist. J. Synchrotron Rad. **2001**, 8, 314–316.
3. Ravel, B.; Newville, M. ATHENA , ARTEMIS , HEPHAESTUS : Data Analysis for X-Ray Absorption

Spectroscopy Using IFEFFIT. J. Synchrotron Rad. **2005**, 12, 537–541.
4. Rudi, S.; Cui, C.; Gan, L.; Strasser, P. Comparative Study of the Electrocatalytically Active Surface Areas (ECSAs) of Pt Alloy Nanoparticles Evaluated by H. Electrocatalysis **2014**, 5, 408–418.
5. Baturina, O. A.; Swider-lyons, K. E. Experimental Methods for Quantifying the Activity of Platinum Electrocatalysts for the Oxygen. Anal. Chem. **2010**, 82 (15), 6321–6328.
6. C. A. Campos-Rold´an, R. G. Gonz´alez-Huerta, and N. A.-V. Experimental Protocol for HOR and ORR in Alkaline Electrochemical Measurements. J. Electrochem. Soc. **2018**, 165 (15), 13001–13007.
7. Wang, J.; Zhao, C.; Liu, J.; Ren, D.; Li, B.; Huang, J.; Zhang, Q. Nano Materials Science Quantitative Kinetic Analysis on Oxygen Reduction Reaction : A Perspective. Nano Mater. Sci. **2021**, 3 (3), 313–318.
8. Kuiken, H. K.; Bakkers, E. P. A. M.; Ligthart, H.; Kelly, J. J. Rotating Ring-Ring Electrode Theory and Experiment The Rotating Ring-Ring Electrode. **2022**, 147 (2000), 1110–1116.
9. Zhou, R.; Zheng, Y.; Jaroniec, M.; Qiao, S. Z. Determination of Electron Transfer Number for Oxygen Determination of Electron Transfer Number for Oxygen Reduction Reaction : From Theory to Experiment. ACS Catal. **2016**, 6 (7), 4720–4728.
10. Tiwari, J. N.; Sultan, S.; Myung, C. W.; Yoon, T.; Li, N.; Ha, M.; Harzandi, A. M.; Park, H. J.; Kim, D. Y.; Chandrasekaran, S. S.; Lee, W. G.; Vij, V.; Kang, H.; Shin, T. J.; Shin, H. S.; Lee, G.; Lee, Z.; Kim, K. S. Multicomponent Electrocatalyst with Ultralow Pt Loading and High Hydrogen Evolution Activity. Nat. Energy **2018**, 3, 773–782.
11. Taehee Kim, Sanjib Baran Roy, Sunil Moon, SangHyuk Yoo, Haryeong Choi, V. G. P.; Younghun Kim, Jihun Lee, Seong Chan Jun, Keonwook Kang, Seung-Hyun Chun, K. K.; Park, and H.-H.; Jun, S. C.; Kang, K.; Chun, S.; Kanamori, K.; Park, H. Highly Dispersed Pt Clusters on F-Doped Tin(IV) Oxide Aerogel Matrix: An Ultra-Robust Hybrid Catalyst for Enhanced Hydrogen Evolution. ACS Nano **2022**, 16, 1625−1638.
12. Persson, P. O. Å.; Rosen, J. X-ray Photoelectron Spectroscopy of Ti3AlC2 , Ti3C2Tz , and TiC Provides Evidence for the Electrostatic Interaction between Laminated Layers in MAX-Phase Materials. J. Phys. Chem. C **2020**, 124 (50), 27732–27742.
13. Yang, C.; Jiang, Q.; Li, W.; He, H.; Yang, L.; Lu, Z.; Huang, H. Ultrafine Pt Nanoparticle-Decorated 3D Hybrid Architectures Built from Reduced Graphene Oxide and MXene Nanosheets for Methanol Oxidation. Chem. Mater. **2019**, 31 (22), 9277–9287.
14. Zhang, C.; Ma, B.; Zhou, Y.; Wang, C. Highly Active and Durable Pt/MXene Nanocatalysts for ORR in Both Alkaline and Acidic Conditions. J. Electroanal. Chem. **2020**, 865, 114142.
15. Yin, Z.; Lu, Z.; Xu, Y.; Zhang, Y.; He, L.; Li, P.; Xiong, L.; Ding, L.; Wei, Y.; Wang, H. Supported MXene/GO Composite Membranes with Suppressed Swelling for Metal Ion Sieving. Membranes (Basel). **2021**, 11, 621.
16. Reza, A.; Simon, H.; Metselaar, C.; Chin, B.; Mehrali, M.; Mehrali, M. MXene/RGO Grafted Sponge with an Integrated Hydrophobic Structure towards Light-Driven Phase Change Composites. Compos. Part B **2023**, 264, 110885.
17. Jeon, I. Y.; Kweon, D. H.; Kim, S. W.; Shin, S. H.; Im, Y. K.; Yu, S. Y.; Ju, M. J.; Baek, J. B. Enhanced Electrocatalytic Performance of Pt Nanoparticles on Triazine-Functionalized Graphene Nanoplatelets for Both Oxygen and Iodine Reduction Reactions. J. Mater. Chem. A **2017**, 5 (41), 21936–21946.
18. Sasaki, K.; Zhang, L.; Adzic, R. R. Niobium Oxide-Supported Platinum Ultra-Low Amount Electrocatalysts for Oxygen Reduction. Phys. Chem. Chem. Phys. **2008**, 10 (1), 159–167. Wang, Y.; Luo, H.; Li, G.; Jiang, J. Highly Active Platinum Electrocatalyst towards Oxygen Reduction Reaction in Renewable Energy Generations of Proton Exchange Membrane Fuel Cells. Appl. Energy **2016**, 173, 59–66.
19. Wang, Y.; Luo, H.; Li, G.; Jiang, J. Highly Active Platinum Electrocatalyst towards Oxygen Reduction Reaction in Renewable Energy Generations of Proton Exchange Membrane Fuel Cells. Appl. Energy **2016**, 173, 59–66. https://doi.org/10.1016/j.apenergy.2016.04.019.
20. Hussain, S.; Erikson, H.; Kongi, N.; Merisalu, M.; Ritslaid, P.; Sammelselg, V.; Tammeveski, K. Heat-Treatment Effects on the ORR Activity of Pt Nanoparticles Deposited on Multi-Walled Carbon Nanotubes Using Magnetron Sputtering Technique. Int. J. Hydrogen Energy **2017**, 42 (9), 5958–5970.
21. Bhuvanendran, N.; Ravichandran, S.; Jayaseelan, S. S.; Xu, Q.; Khotseng, L.; Su, H. Improved Bi-

Functional Oxygen Electrocatalytic Performance of Pt–Ir Alloy Nanoparticles Embedded on MWCNT with Pt-Enriched Surfaces. Energy **2020**, 211, 118695.

22. Xu, C.; Fan, C.; Zhang, X.; Chen, H.; Liu, X.; Fu, Z.; Wang, R.; Hong, T.; Cheng, J. MXene ($Ti_3C_2T_x$) and Carbon Nanotube Hybrid-Supported Platinum Catalysts for the High-Performance Oxygen Reduction Reaction in PEMFC. ACS Appl. Mater. Interfaces, **2020**, 12 (17), 19539−19546.
23. Faraji, M.; Parsaee, F.; Kheirmand, M.; Facile fabrication of N-doped graphene/ Ti3C2Tx (Mxene) aerogel with excellent electrocatalytic activity toward oxygen reduction reaction in fuel cells and metal-air batteries. J. Solid State Chem., **2021**, 303, 122529.
24. Zhang, C.; Ma, B.; Zhou, Y.; Wang, C. Highly Active and Durable Pt/MXene Nanocatalysts for ORR in Both Alkaline and Acidic Conditions. J. Electroanal. Chem. **2020**, 865, 114142.
25. Zhang, Z.; Liu, C.; Dai, Y.; Liu, B.; Guo, P.; Tu, F.; Ma, M.; Shen, L.; Zhao, Z.; Liu, Y.; Zhang, Y.; Zhao, L.; Wang, Z. Sandwich-Structured MXene/Carbon Hybrid Support Decorated with Pt Nanoparticles for Oxygen Reduction Reaction. ACS Appl. Energy Mater. **2022**, 5 (12), 14957–14965.
26. Lei, Y.; Tan, N.; Zhu, Y.; Huo, D.; Sun, S.; Zhang, Y.; Gao, G. Synthesis of Porous N-Rich Carbon/MXene from MXene@Polypyrrole Hybrid Nanosheets as Oxygen Reduction Reaction Electrocatalysts. J. Electrochem. Soc. **2020**, 167 (11), 116503.
27. Peng, X.; Zhao, S.; Mi, Y.; Han, L.; Liu, X.; Qi, D.; Sun, J.; Liu, Y.; Bao, H.; Zhuo, L.; Xin, H. L.; Luo, J.; Sun, X. Trifunctional Single-Atomic Ru Sites Enable Efficient Overall Water Splitting and Oxygen Reduction in Acidic Media. Small **2020**, 16 (33), 1–10.
28. Yang, X.; Jia, Q.; Duan, F.; Hu, B.; Wang, M.; He, L.; Song, Y.; Zhang, Z. Multiwall Carbon Nanotubes Loaded with $MoS_2$ Quantum Dots and MXene Quantum Dots: Non–Pt Bifunctional Catalyst for the Methanol Oxidation and Oxygen Reduction Reactions in Alkaline Solution. Appl. Surf. Sci. **2019**, 464, 78–87.
29. Wang, W. T.; Batool, N.; Zhang, T. H.; Liu, J.; Han, X. F.; Tian, J. H.; Yang, R. When MOFs Meet MXenes: Superior ORR Performance in Both Alkaline and Acidic Solutions. J. Mater. Chem. A **2021**, 9 (7), 3952–3960.
30. Liu, J.; Jiao, M.; Lu, L.; Barkholtz, H. M.; Li, Y.; Jiang, L.; Wu, Z.; Liu, D. J.; Zhuang, L.; Ma, C.; Zeng, J.; Zhang, B.; Su, D.; Song, P.; Xing, W.; Xu, W.; Wang, Y.; Jiang, Z.; Sun, G. High Performance Platinum Single Atom Electrocatalyst for Oxygen Reduction Reaction. Nat. Commun. **2017**, 8 (May), 1–9.
31. Gong, Q.; Gong, S.; Zhang, T.; Cheng, X.; Li, H. Achieving High Activity and Stability of Carbon Supported Pd-Cu Alloyed Catalysts for Fuel Cell Applications. J. Electrochem. Soc. **2019**, 166 (13), F906–F913.
32. Liu, J.; Mi, L.; Xing, Y.; Wang, T.; Wang, F. Construction of $Ti_3C_2$ Supported Hybrid $Co_3O_4$/NCNTs Composite as an Efficient Oxygen Reduction Electrocatalyst. Renew. Energy **2020**, 160, 1168–1173.
33. Feng, Y.; Yang, C.; Fang, W.; Huang, B.; Shao, Q.; Huang, X. Anti-Poisoned Oxygen Reduction by the Interface Modulated Pd@NiO Core@shell. Nano Energy **2019**, 58 (January), 234–243.
34. Eid, K.; Wang, H.; Malgras, V.; Alothman, Z. A.; Yamauchi, Y.; Wang, L. Trimetallic PtPdRu Dendritic Nanocages with Three-Dimensional Electrocatalytic Surfaces. J. Phys. Chem. C **2015**, 119 (34), 19947–19953.
35. Yu X., Yin W., Wang T., Zhang Y. Decorating g-$C_3N_4$ Nanosheets with $Ti_3C_2$ MXene Nanoparticles for Efficient Oxygen Reduction Reaction. Langmuir. **2019**; 35, 2909–2916.
36. Yang X., Jia Q., Duan F., Hu B., Wang M., He L., Song Y., Zhang Z. Multiwall carbon nanotubes loaded with $MoS_2$ quantum dots and MXene quantum dots: Non–Pt bifunctional catalyst for the methanol oxidation and oxygen reduction reactions in alkaline solution. Appl. Surf. Sci. **2019**, 464, 78–87.
37. Li, S.; Que, X.; Chen, X.; Lin, T.; Sheng, L.; Peng, J.; Li, J.; Zhai, M. One-Step Synthesis of Modified $Ti_3C_2$ MXene-Supported Amorphous Molybdenum Sulfide Electrocatalysts by a Facile Gamma Radiation Strategy for Efficient Hydrogen Evolution Reaction. ACS Appl. Energy Mater. **2020**, 3 (11), 10882–10891.
38. Saha, S.; Martin, B.; Leonard, B.; Li, D. Probing Synergetic Effects between Platinum Nanoparticles Deposited: Via Atomic Layer Deposition and a Molybdenum Carbide Nanotube Support through Surface Characterization and Device Performance. J. Mater. Chem. A **2016**, 4 (23), 9253–9265.

39. Hunt, S. T.; Milina, M.; Wang, Z.; Román-Leshkov, Y. Activating Earth-Abundant Electrocatalysts for Efficient, Low-Cost Hydrogen Evolution/Oxidation: Sub-Monolayer Platinum Coatings on Titanium Tungsten Carbide Nanoparticles. Energy Environ. Sci. **2016**, 9 (10), 3290–3301.
40. Zeng, X.; Shui, J.; Liu, X.; Liu, Q.; Li, Y.; Shang, J.; Zheng, L.; Yu, R. Single-Atom to Single-Atom Grafting of $Pt_1$ onto Fe-$N_4$ Center: $Pt_1$@Fe-N-C Multifunctional Electrocatalyst with Significantly Enhanced Properties. Adv. Energy Mater. **2018**, 8 (1), 1–8.
41. Kalasapurayil Kunhiraman, A.; Ramasamy, M.; Ramanathan, S. Efficient Hydrogen Evolution Catalysis Triggered by Electrochemically Anchored Platinum Nano-Islands on Functionalized-MWCNT. Int. J. Hydrogen Energy **2017**, 42 (15), 9881–9891.
42. Ashassi-Sorkhabi, H.; Rezaei-Moghadam, B.; Asghari, E.; Bagheri, R.; Hosseinpour, Z. Fabrication of Bridge like Pt@MWCNTs/$CoS_2$ Electrocatalyst on Conductive Polymer Matrix for Electrochemical Hydrogen Evolution. Chem. Eng. J. **2017**, 308, 275–288.
43. Heydari-Bafrooei, E.; Askari, S. Electrocatalytic Activity of MWCNT Supported Pd Nanoparticles and $MoS_2$ Nanoflowers for Hydrogen Evolution from Acidic Media. Int. J. Hydrogen Energy **2017**, 42 (5), 2961–2969.
44. Yuan Y.; Li H.; Wang L.; Zhang L.; Shi D.; Hong Y.; Sun J.; Achieving highly efficient catalysts for hydrogen evolution reaction by electronic state modification of platinum on versatile Ti3C2T x (MXene). ACS Sustainable Chem Eng, **2019**, 7, 4266e73.
45. Yoon Y.; Tiwari AP.; Lee M.; Choi M.; Song W.; Im J.; Zyung T.; Jung H. K.; Lee S. S.; Jeon S.; An K. S.; Enhanced electrocatalytic activity by chemical nitridation of two-dimensional titanium carbide MXene for hydrogen evolution. J Mater Chem **2018**, 6, 20869e77.
46. Lv Z, Wang M, Liu D, Jian K, Zhang R, Dang J. Synergetic effect of Ni2P and MXene enhances catalytic activity in the hydrogen evolution reaction. Inorg Chem **2021**; 60(3):1604e11.
47. Le TA, Bui QV, Tran NQ, Cho Y, Hong Y, Kawazoe Y, Lee H. Synergistic effects of nitrogen doping on MXene for enhancement of hydrogen evolution reaction. ACS Sustainable Chem Eng **2019**, 7, 16879e88.
48. Thirumal, V., R. Yuvakkumar, P. Senthil Kumar, G. Ravi, A. Arun, Ramesh K. Guduru, and Dhayalan Velauthapillai. "Heterostructured two dimensional materials of MXene and graphene by hydrothermal method for efficient hydrogen production and HER activities." International Journal of Hydrogen Energy 2023, 48, 6478-6487.
49. Yan L., Song D., Liang J., Li X., Li H., Liu Q. Fabrication of highly efficient Rh-doped cobalt–nickel-layered double hydroxide/MXene-based electrocatalyst with rich oxygen vacancies for hydrogen evolution, J. Colloid Interface Sci., 2023, **640**, 338–347.
50. Shen, B., Huang, H., Jiang, Y., Xue, Y. and He, H., 3D interweaving MXene–graphene network–confined Ni–Fe layered double hydroxide nanosheets for enhanced hydrogen evolution. Electrochimica Acta, **2022** 407, 139913.
51. Zhang, X.; Shao, B.; Sun, Z.; Gao, Z.; Qin, Y.; Zhang, C.; Cui, F.; Yang, X. Platinum Nanoparticle-Deposited $Ti_3C_2Tx$ MXene for Hydrogen Evolution Reaction. Ind. Eng. Chem. Res. **2020**, 59, 1822–1828.
52. Cui, C.; Cheng, R.; Zhang, H.; Zhang, C.; Ma, Y.; Shi, C.; Fan, B.; Wang, H.; Wang, X. Ultrastable MXene@Pt/SWCNTs' Nanocatalysts for Hydrogen Evolution Reaction. Adv. Funct. Mater. **2020**, 30, 200693.
53. Tang, Y.; Yang, C.; Sheng, M.; Yin, X.; Que, W. Synergistically Coupling Phosphorus-Doped Molybdenum Carbide with MXene as a Highly Efficient and Stable Electrocatalyst for Hydrogen Evolution Reaction. ACS Sustain. Chem. Eng. **2020**, 8, 12990–12998.
54. Filip, J.; Zavahir, S.; Lorencova, L.; Bertok, T.; Yousaf, A.B.; Mahmoud, K.A.; Tkac, J.; Kasak, P. Tailoring Electrocatalytic Properties of Pt Nanoparticles Grown on $Ti_3C_2T_x$ MXene Surface. J. Electrochem. Soc. **2019**, 166, H54–H62.
55. Ramalingam, V.; Varadhan, P.; Fu, H.C.; Kim, H.; Zhang, D.; Chen, S.; Song, L.; Ma, D.; Wang, Y.; Alshareef, H.N.; et al. Hau. Heteroatom-Mediated Interactions between Ruthenium Single Atoms and an MXene Support for Efficient Hydrogen Evolution. Adv. Mater. **2019**, 31, 1903841.
56. Zhang, J.; Zhao, Y.; Guo, X.; Chen, C.; Dong, C.L.; Liu, R.S.; Han, C.P.; Li, Y.; Gogotsi, Y.; Wang, G.

Single platinum atoms immobilized on an MXene as an efficient catalyst for the hydrogen evolution reaction. Nat. Catal. **2018**, 1, 985–992.
57. Cui, C.; Cheng, R.; Zhang, C.; Wang, X. Pt immobilized spontaneously on porous MXene/MAX hybrid monolith for hydrogen evolution reaction. Chin. Chem. Lett. **2020**, 31, 988–991.
58. Jiang, Y.; Wu, X.; Yan, Y.; Luo, S.; Li, X.; Huang, J.; Zhang, H.; Yang, D. Coupling PtNi Ultrathin Nanowires with MXenes for Boosting Electrocatalytic Hydrogen Evolution in Both Acidic and Alkaline Solutions. Small **2019**, 15, 1805474.
59. Wu, X.; Wang, Z.; Yu, M.; Xiu, L.; Qiu, J. Stabilizing the MXenes by Carbon Nanoplating for Developing Hierarchical Nanohybrids with Efficient Lithium Storage and Hydrogen Evolution Capability. Adv. Mater. **2017**, 29, 1607017.